Seeded free-electron laser driven by a compact laser plasma accelerator

Marie Labat (✉ marie.labat@synchrotron-soleil.fr)
Synchrotron SOLEIL

Jurjen Couperus Cadabag
HZDR   https://orcid.org/0000-0001-9129-4208

Amin Ghaith
Synchrotron Soleil / HZDR

Arie Irman
Helmholtz-Zentrum Dresden-Rossendorf   https://orcid.org/0000-0002-4626-0049

Anthony Berlioux
Synchrotron SOLEIL

Philippe Berteaud
Synchrotron SOLEIL

Frédéric Blache
Synchrotron SOLEIL

Stefan Bock
Helmholtz-Zentrum Dresden - Rossendorf   https://orcid.org/0000-0002-1919-8585

François Bouvet
Synchrotron SOLEIL

Fabien Briquez
Synchrotron SOLEIL

Yen-Yu Chang
HZDR

Sébastien Corde
LOA

Alexander Debus
HZDR

Carlos De Oliveira
Synchrotron SOLEIL

Jean-Pierre Duval
Synchrotron SOLEIL

Yannick Dietrich
Synchrotron SOLEIL

Moussa El Ajjouri

Synchrotron SOLEIL

Christoph Eisenmann

HZDR

Julien gautier

LOA   https://orcid.org/0000-0002-7330-0309

René Gebhardt

Helmholtz-Zentrum Dresden - Rossendorf

Simon Grams

HZDR

Uwe Helbig

Helmholtz-Zentrum Dresden - Rossendorf

Christian Herbeaux

Synchrotron SOLEIL

Nicolas Hubert

Synchrotron SOLEIL

Charles Kitegi

Synchrotron SOLEIL

Olena Kononenko

LOA

Michael Kuntzsch

HZDR

Maxwell LaBerge

HZDR/Univ. of Texas

Stéphane Lé

Synchrotron SOLEIL

Bruno Leluan

Synchrotron SOLEIL

Alexandre Loulergue

Synchrotron SOLEIL

Victor Malka

Weizmann Institute of Science   https://orcid.org/0000-0002-0488-2587

Fabrice Marteau

Synchrotron SOLEIL

Manh Huy N Guyen

Synchrotron SOLEIL

Driss Oumbarek-Espinos

Synchrotron SOLEIL

Richard Pausch

HZDR

Damien Pereira
Synchrotron SOLEIL

Thomas Püschel
Helmholtz-Zentrum Dresden - Rossendorf   https://orcid.org/0000-0002-4738-6436

Jean-Paul Ricaud
Synchrotron SOLEIL

Patrick Rommeluere
Synchrotron SOLEIL

Eleonore Roussel
Laboratoire PhLAM   https://orcid.org/0000-0002-4245-6781

Pascal Rousseau
LOA

Susanne Schöbel
HZDR/Technische Universität Dresden   https://orcid.org/0000-0002-2769-4749

Mourad Sebdaoui
Synchrotron SOLEIL

Klaus Steiniger
HZDR

Keihan Tavakoli
Synchrotron SOLEIL

Cedric Thaury
ENSTA/CNRS/ECOLE POLYTECHNIQUE   https://orcid.org/0000-0002-6537-8392

Patrick Ufer
HZDR/Technische Universität Dresden

Mathieu Valléau
Synchrotron SOLEIL

Marc Vandenberghe
Synchrotron SOLEIL

José Vétéran
Synchrotron SOLEIL

Ulrich Schramm
Helmholtz-Zentrum Dresden - Rossendorf   https://orcid.org/0000-0003-0390-7671

Marie Couprie
Soleil Synchrotron   https://orcid.org/0000-0001-5073-0181

Physical Sciences - Article

Keywords:

Seeded free-electron laser driven by a compact laser plasma accelerator

Marie Labat[†,1,∗] Jurjen Couperus Cabadağ,[2,†] Amin Ghaith,[2,1,†] Arie Irman,[2,†] Anthony Berlioux,[1] Philippe
Berteaud,[1] Frédéric Blache,[1] Stefan Bock,[2] François Bouvet,[1] Fabien Briquez,[1] Yen-Yu Chang,[2] Sébastien
Corde,[3] Alexander Debus,[2] Carlos De Oliveira,[1] Jean-Pierre Duval,[1] Yannick Dietrich,[1] Moussa El
Ajjouri,[1] Christoph Eisenmann,[2] Julien Gautier,[3] René Gebhardt,[2] Simon Grams,[2] Uwe Helbig,[2] Christian
Herbeaux,[1] Nicolas Hubert,[1] Charles Kitegi,[1] Olena Kononenko,[3] Michael Kuntzsch,[2] Maxwell LaBerge,[2,4]
Stéphane Lé,[1] Bruno Leluan,[1] Alexandre Loulergue,[1] Victor Malka,[3,‡] Fabrice Marteau,[1] Manh
Huy N Guyen,[1] Driss Oumbarek-Espinos,[1,§] Richard Pausch,[2] Damien Pereira,[1] Thomas Püschel,[2]
Jean-Paul Ricaud,[1] Patrick Rommeluere,[1] Eléonore Roussel,[5] Pascal Rousseau,[3] Susanne Schöbel,[2,6]
Mourad Sebdaoui,[1] Klaus Steiniger,[2] Keihan Tavakoli,[1] Cédric Thaury,[3] Patrick Ufer,[2,6] Mathieu
Valléau,[1] Marc Vandenberghe,[1] José Vétéran,[1] Ulrich Schramm,[2,6] and Marie-Emmanuelle Couprie[1]

[1]*Synchrotron SOLEIL, L'Orme des Merisiers, 91191 Gif-sur-Yvette, France*
[2]*Helmholtz-Zentrum Dresden - Rossendorf, Bautzner Landstrasse 400, 01328 Dresden, Germany*
[3]*LOA, ENSTA Paris, CNRS, Ecole Polytechnique,*
Institut Polytechnique de Paris, 91762 Palaiseau, France
[4]*The University of Texas at Austin, Austin, TX 78712-1081, USA*
[5]*Univ. Lille, CNRS, UMR 8523–PhLAM–Physique des Lasers Atomes et Molécules, F–59000 Lille, France*
[6]*Technische Universität Dresden, 01062 Dresden, Germany*

∗ marie.labat@synchrotron-soleil.fr
† These authors contributed equally to this work
‡ Current address: Department of Physics of Complex Systems, Weizmann Institute of Science, Rehovot 76100, Israel
§ Current address: Institute of Scientific and Industrial Research, Osaka University, 8-1 Mihogaoka, Ibaraki, Osaka, 567-0047, Japan

Free-electron lasers generate high-brilliance coherent radiation at wavelengths spanning from the infrared to the X-ray domains. The recent development of short-wavelength seeded free-electron lasers now allows for unprecedented levels of control on longitudinal coherence [1], opening new scientific avenues as ultra-fast dynamics on complex systems and X-ray nonlinear optics. While those devices rely on state-of-the-art large-scale accelerators, advancements on laser-plasma accelerators, which harness giga-volt-per-centimeter accelerating fields, showcase a promising technology as compact drivers for free-electron lasers. Using such miniaturized accelerators, exponential amplification of a shot-noise type of radiation in a self-amplified spontaneous emission configuration was recently achieved [2]. However, employing this compact approach for the delivery of temporally coherent pulses in a controlled manner remained a major challenge. Here, we present the experimental demonstration of a laser-plasma accelerator driven free-electron laser in a seeded configuration, where control over the radiation wavelength is accomplished. Furthermore, the appearance of interference fringes, resulting from the interaction between the phase-locked emitted radiation and the seed, confirms longitudinal coherence. Building on our scientific achievements, we anticipate a straightforward scaling to extreme-ultraviolet wavelengths, paving the way towards university-scale free-electron lasers, unique tools for a multitude of applications.

Research and daily life have been profoundly impacted by the invention of the laser. Until today, this impact even grows with the expansion of available parameters thanks to innovations in system design and gain media. With the advent of ultra-short pulse and high peak power technology based on chirped pulse amplification (CPA) [3], lasers literally pushed the frontiers of science, opening the door to new applications in relativistic-intensity laser-matter interaction [4], for which laser-plasma acceleration [5] is a prominent example. Fundamental limitations however remain for the generation of hard radiation as light amplification is based on population inversion of electronic states in typically solid state material. Free-Electron Lasers (FELs) [6] in contrast harness a completely different gain medium: relativistic electron beams wiggling in a periodically alternating magnetic field. FELs experienced game-changing progress over the past decades. The first infrared FELs providing pJ pulse energies [7] paved the way to hard X-ray tunable systems [8, 9]. FEL applications advanced simultaneously and X-ray FELs are now established as unique high brillance tools for the investigation of matter with atomic resolution at femto- to attosecond time scales [1]. This progress was enabled by continuous improvements in electron beam driver quality, mainly supported in view of the next generation of particle colliders. However, such state-of-the-art linear accelerators are typically hundreds of meters long and involve high investment and operational costs. With their unprecedented accelerating fields, Laser-Plasma Accelerators (LPAs) [10] appeared as alternative drivers [11] promising a down-scaling in size by more than one order of magnitude. Thus, the realization of a compact LPA-driven FEL has been identified as one of the major challenges of this decade, for example adressed via EuPRAXIA [12] in the European Strategic Forum for Research Infrastructure (ESFRI) roadmap.

In FELs, the wiggling relativistic electron beam interacts with a co-propagating radiation at the resonant undulator wavelength $\lambda_R = \lambda_u \times (1 + K_u^2/2)/(2\gamma^2)$, with γ being the Lorentz factor of the electron beam, λ_u the undulator period and K_u its deflection parameter. This interaction leads to an energy modulation further converted into a density modulation of the electron bunch at λ_R initiating a coherent emission process scaling quadratically with the bunch charge. FEL radiation is spectrally tunable via the electron energy and the deflection parameter. Contrary to oscillator [13] and self-amplified spontaneous emission (SASE) [14] configurations, in which the radiation starts from the spontaneous synchrotron (undulator) radiation, a seeded configuration employs an external coherent source or a monochromatized upstream SASE pulse tuned to λ_R. SASE FELs can provide gigawatt level peak power pulses with a high degree of transverse coherence. They however suffer from low longitudinal coherence since their radiation starts from shot-noise, generally exhibiting spiky temporal and spectral distributions. To mitigate these issues, external seeding was proposed [15, 16] and rapidly revealed as a powerful strategy to control pulse shape and to guarantee longitudinal coherence [17, 18] even down to very short wavelengths [16, 19–22]. Presently, most XUV and X-ray

FELs can be externally or self-seeded to provide the highest level of spectral purity [23, 24] and the possibility to tailor emission properties [25, 26].

LPAs rely on ultra-short and relativistic intensity laser pulses focused into underdense plasma to excite μm-scale collective plasma oscillations, traveling with nearly the speed of light in the wake of the drive laser pulse. In contrast to cavity based accelerators, LPAs are not limited by vacuum break-down and their acceleration gradients can reach several hundreds of GV/m. LPAs rapidly developed, involving extensive research on high-quality injection and acceleration schemes [27], plasma targets, drive laser technologies [28] and diagnostics [29]. They now feature electron bunches with optimized parameters as energies up to 8 GeV [30], emittances down to 0.1 mm.mrad [31], sub-percent energy spread [32] and nanocoulomb charges [33, 34] with durations typically around 10 fs [35, 36] sustaining several tens of kA peak currents [33, 36, 37], all with improved stability [38].

LPAs now sets the stage to drive university-scale FELs. After the development of LPA beam manipulation strategies [39, 40] and the observation of spontaneous emission [41–45], the first SASE FEL amplification driven by an LPA was reported [2, 46] at a wavelength of 27 nm. As SASE radiation still inherently lacks temporal coherence, in this work we aim at the experimental demonstration of a seeded LPA powered FEL. Using an external seed at 270 nm, we achieve control of the radiated wavelength, taking advantage of the energy and wavelength chirps of both the electron and the seed laser beams, respectively. Longitudinal coherence is substantiated by the observation of phase-locked interference fringes between the seed and the FEL pulses. These experimental results are supported quantitatively by both numerical simulations and analytical modeling.
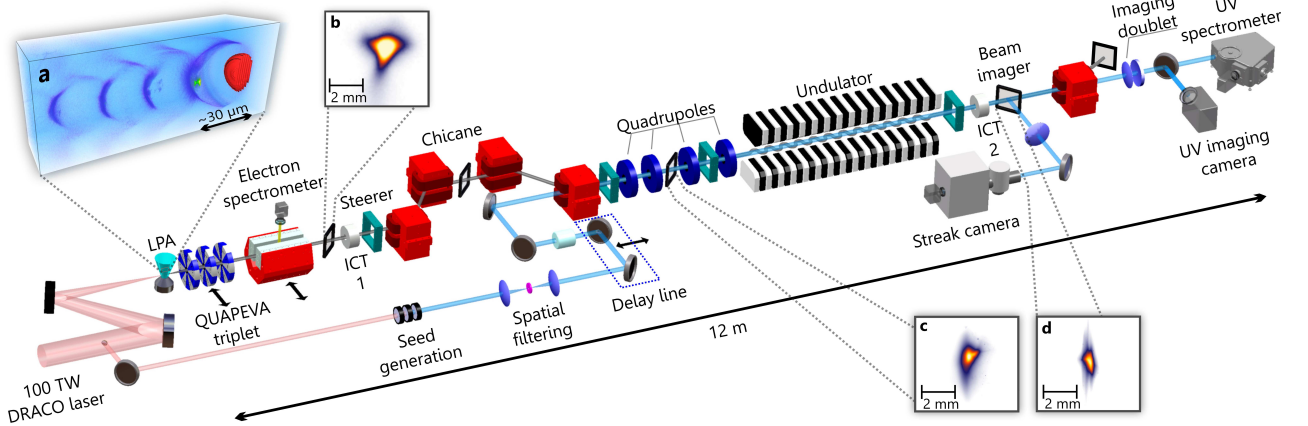

FIG. 1. **Experimental layout.** The electron beam generated in the LPA is first characterized using a removable electron spectrometer and then sent through a triplet of quadrupoles (QUAPEVAs) for beam transport to the undulator and FEL radiation generation. ICTs: Integrated Current Transformers. Non-labelled elements: dipoles (*red blocks*), optical lenses (*blue*), mirrors (*grey circled black disks*). Inset **a**: Particle-in-Cell simulation renders of the accelerating structure driven by the laser pulse (*red*), the electron cavity sheet formed from the plasma medium (*light blue*) is visible in *purple* and the accelerated electron bunch visible in *green*. Insets **b,c,d**: Electron beam transverse distribution measured at LPA exit (**b**), at undulator entrance (**c**) and at undulator exit (**d**).

Experimental setup. The experiment was performed at the Helmholtz-Zentrum Dresden-Rossendorf, combining the LPA driven by the 100 TW-class arm of the DRACO laser [47] with the COXINEL beam manipulation line [48]. A schematic of the experimental layout is given in Fig. 1. The LPA is operated in a tailored self-truncated ionization-induced injection scheme [49] employing beam loading to limit the energy spread [33]. The LPA performance is optimized for high spectral charge density and low divergence beams. Discarding off-energy and low charge density shots which cannot lead to FEL observation (see Extended Data Fig. 5), electron beams exhibit a peak energy E_e at 188 MeV with a statistical standard deviation (s.d.) of 6 MeV, a relative energy spread σ_E of 6.3%–RMS $\pm 0.8\%$ s.d., resulting in a spectral charge density of 6.3 pC/MeV–FWHM ± 1.3 pC/MeV s.d., with a mean horizontal divergence $\sigma_{x'}$ of 0.8 mrad–RMS ± 0.2 mrad s.d. throughout a $\pm 5\%$ energy band (180–198 MeV). The electron beam duration σ_z can
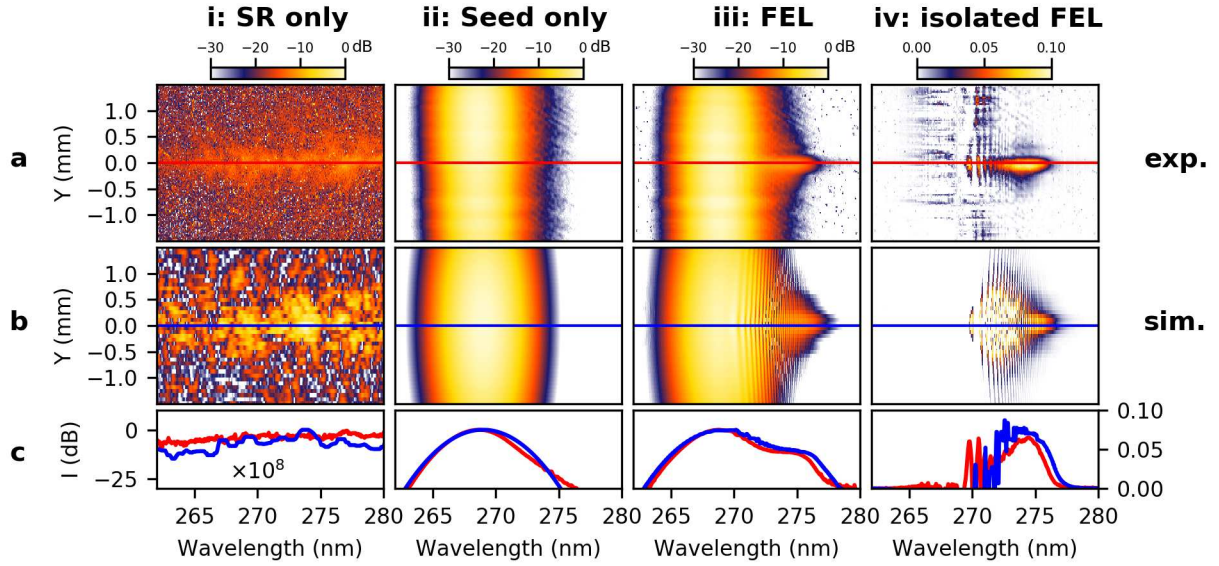
FIG. 2. **Spatio–spectral distributions of the radiation at the undulator exit**. **a,b**, Spatio–spectral distributions for an undulator gap of 4.3 mm ($K_u = 2.35$) and an optimum delay of +0.1 ps. Experimental measurement (**a**) and simulation (**b**) of synchrotron radiation (SR) only (**i**), seed only (**ii**), synchrotron radiation with seed (**iii**) and difference between (**iii**) and (**ii**) images (**iv**). In (**a,b - i,ii,iii**): distributions normalized to their maximum intensity and displayed in logarithmic (dB) scale. In (**a,b - iv**): distributions displayed in linear scale. **c**, On–axis spectral intensity extracted along red line in (**a**) and blue line in (**b**) images with integration over Δy=0.3 mm and median filtering of the simulated profile. Simulation parameters (electron beam parameters given at source point): $E_e = 188.8$ MeV, charge = 150 pC, $\sigma_z = 2\mu$m–RMS, normalized emittance $\epsilon_{x,y}$=(1.5;1.0) mm.mrad, divergence $\sigma_{x',y'}$=(1.5;1.0) mrad–RMS, $\sigma_e = 5\%$–RMS, R_{56}=1.8 mm, QUAPEVA 2 strength detuned by -2%, E_{seed}=0.5 μJ, λ_{seed}=269 nm, $\Delta\lambda_{seed}$=3.9 nm–FWHM, ΔT_{seed}=1.0 ps–FWHM.

92 be estimated around 14.8 fs-FWHM ±1.6 fs s.d. based on previous measurements [36]. With the spectrometer removed,
93 the electron beam is transported through the COXINEL beamline [48]. A triplet of tunable high gradient quadrupoles
94 (QUAPEVAs), located behind the LPA, first handles the electron beam divergence for chromatic emittance growth
95 mitigation. The beam is then decompressed in a four-dipole-magnet chicane. For a nominal chicane strength R_{56}
96 of 1.8 mm, the chicane stretches the beam up to 0.9 ps-FWHM while imposing an energy-position correlation (chirp)
97 according to $\gamma(t) = \gamma_0(1 + ct/R_{56})$, with t the longitudinal position along the beam with respect to the central energy
98 γ_0 location and c the speed of light. Subsequently, four quadrupoles create a chromatic sliding focusing [40] of the
99 electrons according to their energy inside an in-vacuum undulator. This undulator consists of 97 periods of 20 mm
100 length with a gap tunable down to 4 mm, providing a maximum deflection parameter K_u of 2.47. Electrons are finally
101 deflected with a dipole, allowing for photon beam diagnostics. The seed is generated by frequency conversion of a
102 small fraction of the driver laser, providing a pulse energy E_{seed} of 0.8 μJ within a bandwidth $\Delta\lambda_{\text{seed}}$ of 3.9 nm–FWHM
103 at a central wavelength λ_0 of 269 nm. To relax the temporal overlap between seed and electron beam, the seed is
104 stretched to an estimated duration ΔT_{seed} of 1 ps–FWHM by introducing dispersion. This stretching induces a strong
105 longitudinal dependence (linear chirp) of the seed wavelength according to $\lambda_{seed}(t) = \lambda_0 + (t - \tau)/D_\lambda$, where τ is
106 the delay with respect to the electron beam maximum charge density location and D_λ is the group delay dispersion.
107 The radiation at the undulator exit is near-field imaged onto a 2D UV-spectrometer, providing 2D spatio-spectral
108 distribution, i.e. vertical position versus spectral distribution.

109 **Seeded FEL demonstration.** The measured spatio-spectral distributions are presented in Fig. 2a. The syn-
110 chrotron radiation only (a-i) exhibits a broadband spectral distribution due to the large electron beam energy spread.
111 The seed radiation only (a-ii) has a nearly Gaussian spatio-spectral distribution with a peak intensity approximately
112 eight orders of magnitude higher than the synchrotron radiation. Once the 3D (spatial, temporal and frequency) over-
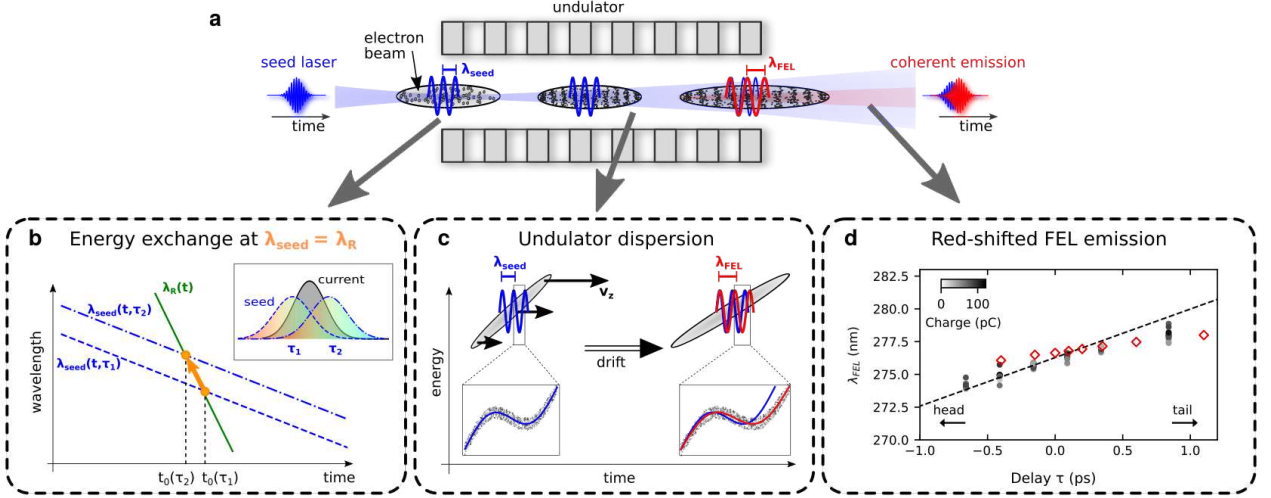113 lap between the electrons and the seed is established inside the undulator (see Methods), an additional red-shifted

FIG. 3. **Principle of seeded FEL and spectral control. a**, Seeded FEL principle: an external seed laser periodically modulates, at its optical wavelength, the electron beam as it travels in the periodic magnetic field of an undulator. The microbunched electron beam finally emits coherent light at the wavelength of the density modulation period. **b**, FEL resonance condition: due to the chirps of the electron beam energy and seed wavelength, energy exchange between the electron beam and the seed laser can only occur at the longitudinal position t_0 where the resonance condition $\lambda_{seed}(t_0) = \lambda_R(t_0)$ is satisfied. This resonance location t_0 is shifted (orange arrow) if the delay τ between the seed and the electron beam is varied. **c**, Undulator dispersion-induced modulation period stretching. As long as the electron beam traverses the undulator, the undulator dispersion induces a stretching of the electron beam. The periodic modulation initiated by the seed laser at the resonant wavelength is thus stretched, leading to an FEL coherent emission red-shifted with respect to the seed laser optical wavelength. **d**, λ_{FEL} versus delay τ (see also Extended Data Fig. 9). $\tau=0$ corresponds to perfect synchronization between the seed and the electron beam. For $\tau < 0$ (resp. $\tau > 0$), the seed arrives before (resp. after) the electron beam at the undulator entrance. Experimental data (grey dots) with color scale representing the charge of each single shot. Delay scan done for a 4.3 mm-undulator gap. Model (black dashed line) from Eq. (1) with $E_e = 188.8$ MeV, $R_{56} = 1.8$ mm, $L_{eff} = 1.87$ m and $D = -0.296$ ps/nm. Simulations (red diamonds) using same parameters as in Fig. 2 except for charge: 100 pC, corresponding to a spectral charge density of 3 pC/MeV.

signal appears (a-iii). To ease its viewing, the seed contribution (a-ii) is subtracted (see Methods), leading to the trace shown in (a-iv). This isolated trace is spectrally red-shifted, by more than 5 nm, with respect to the seed. The experimental spatio-spectral distributions (Fig. 2a) and on-axis spectral intensities detailed as line-outs in Fig. 2c are found to be in very good agreement with simulations (see Methods) depicted in Fig. 2b. The isolated red-shifted trace exhibited in Fig. 2iv evidences seeded FEL operation, following the prediction of [50].

The fundamental mechanism leading to this red-shift is illustrated in Fig. 3. In a seeded configuration (Fig. 3a), the first step of the FEL process is energy exchange between seed and electron beam at the resonance wavelength. Since both the seed wavelength and the electron beam energy are time dependent, the resonant condition $\lambda_{seed}(t) = \lambda_R(t)$ can only be met at one longitudinal position t_0 (see Fig. 3b and Methods). This local energy exchange at t_0 leads to an energy and further density modulation of the electrons at $\lambda_{seed}(t_0)$ (or $\lambda_R(t_0)$), expected to be followed by a coherent emission at the same wavelength. However, if at the scale of one modulation period, the electrons energy varies significantly, which is the case due to the strong electron beam chirp, the initial density modulation period is stretched by the dispersion experienced along the undulator. This leads to a lengthening of the coherent emission wavelength (Fig. 3c), i.e. a red-shift [50]. According to this model, the final seeded FEL wavelength is expected to behave as:

$$\lambda_{FEL} = \left(\lambda_0 + \frac{t_0 - \tau}{D_\lambda}\right) \times \left(1 + \frac{1 + K_{u0}^2/2}{\gamma(t_0)^2 R_{56}} L_{eff}\right) \tag{1}$$

where K_{u0} is the deflection parameter ensuring resonance at $\tau=0$ and L_{eff} is the effective undulator length along

which the modulation period stretching takes place. The isolated trace exhibited in Fig. 2a-iv is red-shifted up to a central wavelength of 274 nm, i.e. well matching the 276 nm prediction of Eq. (1) using L_{eff}=1.9 m. This absolute agreement confirms the observation of a seeded FEL.

FEL spectral control. The measured λ_{FEL} as a function of the delay τ is shown in Fig. 3d. Beyond $\tau=\pm1$ ps, the FEL signal disappears. With the seed pulse longitudinally sweeping the electron beam distribution, this ±1 ps interval is in good agreement with the convolution between two ≈ 1 ps-FWHM pulses (seed and electron beam). Within the observation range, λ_{FEL} correlates linearly with τ, in good agreement with simulations, accurately following the prediction of Eq. (1). These results show that the FEL wavelength is locked thanks to the external seeding and can be fully controlled by the electron beam and seed chirps.
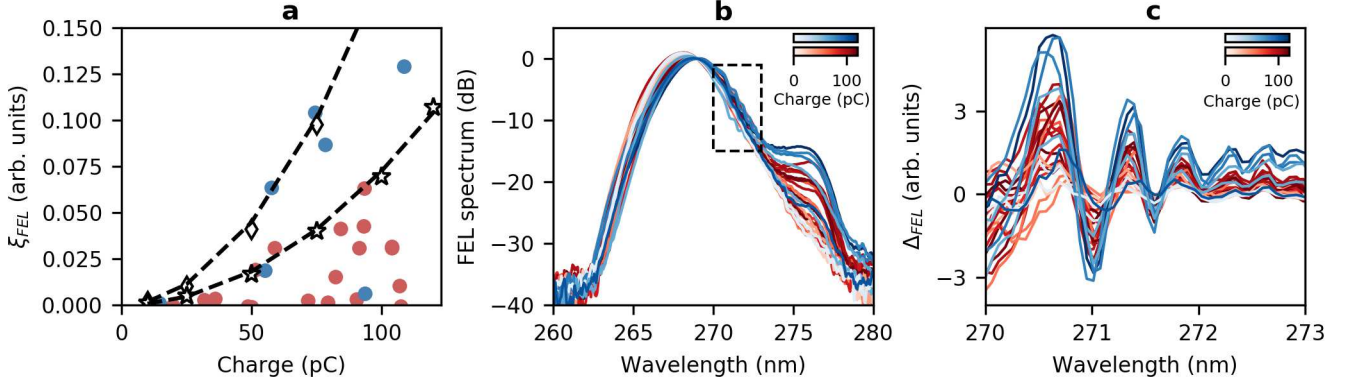

FIG. 4. **FEL quadratic charge dependence and longitudinal coherence. a**, ξ_{FEL} versus charge measured at beamline exit (see Extended Data Fig. 6) using two sets of data both recorded at optimum gap (4.3 mm) and optimum delay (τ=+0.1 ps): first set recorded (*blue dots*), second set recorded one hour later (*red dots*). Simulated ξ_{FEL} versus charge using $\sigma_e = 5\%$–RMS with a total charge of 100 pC, i.e. spectral charge density of 3 pC/MeV (*black diamonds*) and $\sigma_e = 7.5\%$–RMS with a total charge of 100 pC, i.e. spectral charge density of 2 pC/MeV (*black stars*) with other parameters of Fig. 2. Quadratic fit of simulated ξ_{FEL} (*black dashed line*) using 1.79×10^{-5} (resp. 7.25×10^{-6}) for first set (resp. second set). **b**, FEL on–axis spectra corresponding to ξ_{FEL} points (**a**) using red and blue color scale according to charge. **c**, Difference between FEL on–axis spectra (**b**) and associated seed on–axis spectra. All experimental data were sorted according to the seed peak intensity, keeping only data for seed intensity in the $\pm10\%$ range around the optimum FEL generation.

Charge dependance. To further classify the FEL emission, a new observable is derived from the isolated trace shown in Fig. 2c-iv: the isolated FEL pulse energy ξ_{FEL} (see Methods). Two sets of ξ_{FEL} measurements are presented in Fig. 4a. For each set, best ξ_{FEL} shots at a given charge are consistent with a quadratic dependance versus beam charge. The first set is well reproduced by simulations using a spectral charge density of 3 pC/MeV, while the second set, recorded one hour later, is matched using 2 pC/MeV, indicating a slight detuning of the LPA performance over time. The shots below the driving quadratic behaviour are attributed to the intrinsic shot-to-shot jitter of the LPA beam, leading to a gain loss and/or to a spatial or spectral mismatch between the seed and the electron beam in the undulator. The upper–limit quadratic charge dependance is a signature of an FEL in the coherent emission regime.

Longitudinal coherence. In Fig. 4b, two sets of measured FEL spectra are shown. First, the FEL wavelength stays locked and is independent of the beam charge as predicted by Eq. (1). Additionally, the spectra exhibit a systematic periodic perturbation spectrally positioned between the seed and the FEL peak intensity (within dashed rectangle). For more thorough study, the seed contribution is removed from the FEL spectra (see Methods) resulting in the Δ_{FEL} trace shown in Fig. 4c. The perturbations unambiguously correspond to interference fringes between seed and FEL pulses [50]. Over the two sets of measurements, both the period and the phase of those fringes remain stable. Such a stability can only be derived from phase-locking between the seed and the FEL pulses, providing conclusive evidence of temporal coherence.

Conclusion. We have demonstrated an LPA-driven seeded FEL. Its radiation is spectrally controlled and, in contrast to SASE, exhibits a defined longitudinal phase correlation adding temporal coherence to this compact light source.

The continuous progress of the LPA beam quality, confirmed here, together with the accuracy of the demonstrator modeling, enables the straightforward scaling of our results to the application-relevant XUV range. Considering a 400 MeV electron beam with parameters as described in [34], together with the current COXINEL beamline upgraded with a 3 m-long cryogenic undulator of 15 mm period (available at SOLEIL) and a seed generated by harmonics in gas, coherent FEL pulses above the gigawatt level are predicted at 40 nm. There is no showstopper for LPA-based seeded FELs down to XUV wavelengths. Still, the path towards compact LPA-driven X-ray FELs, remains challenging. Stringent electron beam parameters have to be met, higher repetition-rate operation and system stability have to be further improved. While these constitute a large community effort in a long-term time scale, our findings represent a key milestone toward controlled, miniaturized university-scale LPA based FELs for applications benefiting from the intrinsic laser-to-FEL pulses synchronization.

Online content

Methods, extended data, acknowledgements, details of author contributions and competing interests are available below.

---

[1] Meyer, M. FELs of europe: Whitebook on science with free electron lasers 8–19 (2016). URL `http://xfel.tind.io/record/1510`.

[2] Wang, W. *et al.* Free-electron lasing at 27 nanometres based on a laser wakefield accelerator. *Nature* **595**, 516–520 (2021).

[3] Strickland, D. & Mourou, G. Compression of amplified chirped optical pulses. *Optics Communications* **55**, 447–449 (1985). URL `http://linkinghub.elsevier.com/retrieve/pii/0030401885901518`.

[4] Albert, F. *et al.* 2020 roadmap on plasma accelerators. *New Journal of Physics* **23**, 031101 (2021). URL `https://doi.org/10.1088/1367-2630/abcc62`.

[5] Tajima, T. & Malka, V. Laser plasma accelerators. *Plasma Physics and Controlled Fusion* **62**, 034004 (2020). URL `https://iopscience.iop.org/article/10.1088/1361-6587/ab6da4`.

[6] Madey, J. M. J. Stimulated emission of bremsstrahlung in a periodic magnetic field. *Journal of Applied Physics* **42**, 1906–1913 (1971). URL `https://doi.org/10.1063/1.1660466`. https://doi.org/10.1063/1.1660466.

[7] Deacon, D. A. G. *et al.* First operation of a free-electron laser. *Phys. Rev. Lett.* **38**, 892–894 (1977). URL `https://link.aps.org/doi/10.1103/PhysRevLett.38.892`.

[8] Emma, P. *et al.* First lasing and operation of an ngstrom-wavelength free-electron laser. *Nature Photonics* **4**, 641–647 (2010).

[9] Decking, W. *et al.* A mhz-repetition-rate hard x-ray free-electron laser driven by a superconducting linear accelerator. *Nature photonics* **14**, 391–397 (2020).

[10] Tajima, T. & Dawson, J. M. Laser Electron Accelerator. *Physical Review Letters* **43**, 267–270 (1979). URL `http://link.aps.org/doi/10.1103/PhysRevLett.43.267`.

[11] Nakajima, K. Towards a table-top free-electron laser. *Nature Physics* **4**, 92–93 (2008).

[12] Assmann, R., Weikum, M., Akhter, T. & et al. Eupreaxia conceptual design report. *Eur. Phys. J. Spec. Top.* **229**, 3675–4284 (2020).

[13] Couprie, M. E. Short wavelength free-electron laser sources. *Comptes Rendus de l'Académie des Sciences-Series IV-Physics* **1**, 329–345 (2000).

[14] Kondratenko, A. & Saldin, E. Generating of coherent radiation by a relativistic electron beam in an ondulator. *Part. Accel.* **10**, 207–216 (1980).

[15] Boscolo, I. & Stagno, V. The converter and the transverse optical klystron. *Nuovo Cimento B Serie* **58B**, 267–285 (1980).

[16] Feldhaus, J., Saldin, E., Schneider, J., Schneidmiller, E. & Yurkov, M. Possible application of x-ray optical elements for reducing the spectral bandwidth of an x-ray sase fel. *Optics Communications* **140**, 341–352 (1997).

[17] Prince, K. C. *et al.* Coherent control with a short-wavelength free-electron laser. *Nature Photonics* **10**, 176–179 (2016).

[18] Gorobtsov, O. Y. *et al.* Seeded x-ray free-electron laser generating radiation with laser statistical properties. *Nature communications* **9**, 4498–4498 (2018).

[19] Lambert, G. *et al.* Injection of harmonics generated in gas in a free-electron laser providing intense and coherent extreme-ultraviolet light. *Nat. Phys.* **4**, 296–300 (2008).

[20] Yu, L.-H. *et al.* High-gain harmonic-generation free-electron laser. *Science* **289**, 932–934 (2000). URL `https://www.science.org/doi/abs/10.1126/science.289.5481.932`. https://www.science.org/doi/pdf/10.1126/science.289.5481.932.

[21] Allaria, E. *et al.* Highly coherent and stable pulses from the fermi seeded free-electron laser in the extreme ultraviolet. *Nature Photonics* **6**, 699704 (2012).

[22] Lutman, A. A. *et al.* Demonstration of single-crystal self-seeded two-color x-ray free-electron lasers. *Phys. Rev. Lett.* **113**, 254801 (2014). URL `https://link.aps.org/doi/10.1103/PhysRevLett.113.254801`.

[23] Inoue, I. *et al.* Generation of narrow-band x-ray free-electron laser via reflection self-seeding. *Nature Photonics* **13**, 319–322 (2019).

[24] Nam, I. *et al.* High-brightness self-seeded x-ray free-electron laser covering the 3.5 kev to 14.6 kev range. *Nature Photonics* **15**, 435–441 (2021).

[25] Ferrari, E. *et al.* Widely tunable two-colour seeded free-electron laser source for resonant-pump resonant-probe magnetic scattering. *Nature Communications* **7**, 10343 (2016). URL `https://hal.sorbonne-universite.fr/hal-01277514`.

[26] Maroju, P. *et al.* Attosecond pulse shaping using a seeded free-electron laser. *Nature* **578** (2020).

[27] Esarey, E., Schroeder, C. B. & Leemans, W. P. Physics of laser-driven plasma-based electron accelerators. *Rev. Mod. Phys.* **81**, 1229–1285 (2009). URL `https://link.aps.org/doi/10.1103/RevModPhys.81.1229`.

[28] Danson, C. N. *et al.* Petawatt and exawatt class lasers worldwide. *High Power Laser Science and Engineering* **7**, e54 (2019).

[29] Downer, M. C., Zgadzaj, R., Debus, A., Schramm, U. & Kaluza, M. C. Diagnostics for plasma-based electron accelerators. *Reviews of Modern Physics* **90**, 035002 (2018). URL `https://doi.org/10.1103/RevModPhys.90.035002https://link.aps.org/doi/10.1103/RevModPhys.90.035002`.

[30] Gonsalves, A. J. *et al.* Petawatt Laser Guiding and Electron Beam Acceleration to 8 GeV in a Laser-Heated Capillary Discharge Waveguide. *Physical Review Letters* **122**, 084801 (2019). URL `https://link.aps.org/doi/10.1103/PhysRevLett.122.084801`.

[31] Plateau, G. R. *et al.* Low-Emittance Electron Bunches from a Laser-Plasma Accelerator Measured using Single-Shot {X}-Ray Spectroscopy. *Physical Review Letters* **109**, 064802 (2012). URL `http://aip.scitation.org/doi/abs/10.1063/1.4773707https://link.aps.org/doi/10.1103/PhysRevLett.109.064802`.

[32] Wang, W. T. *et al.* High-Brightness High-Energy Electron Beams from a Laser Wakefield Accelerator via Energy Chirp Control. *Physical Review Letters* **117**, 124801 (2016). URL `https://link.aps.org/doi/10.1103/PhysRevLett.117.124801`.

[33] Couperus, J. P. *et al.* Demonstration of a beam loaded nanocoulomb-class laser wakefield accelerator. *Nature Communications* **8**, 487 (2017). URL `https://www.nature.com/articles/s41467-017-00592-7.pdfhttp://www.nature.com/articles/s41467-017-00592-7`.

[34] Götzfried, J. *et al.* Physics of High-Charge Electron Beams in Laser-Plasma Wakefields. *Physical Review X* **10**, 041015 (2020). URL `https://doi.org/10.1103/PhysRevX.10.041015https://link.aps.org/doi/10.1103/PhysRevX.10.041015`.

[35] Lundh, O. *et al.* Few femtosecond, few kiloampere electron bunch produced by a laserplasma accelerator. *Nature Physics* **7**, 219–222 (2011). URL `http://dx.doi.org/10.1038/nphys1872http://www.nature.com/doifinder/10.1038/nphys1872http://www.nature.com/articles/nphys1872`.

[36] Zarini, O. *et al.* Multioctave high-dynamic range optical spectrometer for single-pulse, longitudinal characterization of ultrashort electron bunches. *Physical Review Accelerators and Beams* **25**, 012801 (2022). URL `https://link.aps.org/doi/10.1103/PhysRevAccelBeams.25.012801`.

[37] Li, Y. F. *et al.* Generation of 20 kA electron beam from a laser wakefield accelerator. *Physics of Plasmas* **24**, 023108 (2017). URL `http://aip.scitation.org/doi/10.1063/1.4975613`.

[38] Maier, A. R. *et al.* Decoding Sources of Energy Variability in a Laser-Plasma Accelerator. *Physical Review X* **10**, 031039 (2020). URL `https://doi.org/10.1103/PhysRevX.10.031039https://link.aps.org/doi/10.1103/PhysRevX.10.031039`.

[39] Maier, A. *et al.* Demonstration scheme for a laser-plasma-driven free-electron laser. *Physical Review X* **2**, 031019 (2012).

[40] Loulergue, A. *et al.* Beam manipulation for compact laser wakefield accelerator based free-electron lasers. *New Journal of Physics* **17**, 023028 (2015). URL `https://doi.org/10.1088/1367-2630/17/2/023028`.

[41] Schlenvoigt, H.-P. *et al.* A compact synchrotron radiation source driven by a laser-plasma wakefield accelerator. *Nature Physics* **4**, 130–133 (2008).

[42] Fuchs, M. *et al.* Laser-driven soft-x-ray undulator source. *Nature Physics, v.5, 826-829 (2009)* **5** (2009).

[43] Anania, M. P. *et al.* An ultrashort pulse ultra-violet radiation undulator source driven by a laser plasma wakefield accelerator. *Applied Physics Letters* **104**, 264102–264102 (2014).

[44] Maier, A. R. *et al.* Water-window x-ray pulses from a laser-plasma driven undulator. *Scientific reports* **10**, 1–8 (2020).

[45] Ghaith, A. *et al.* Tunable high spatio-spectral purity undulator radiation from a transported laser plasma accelerated electron beam. *Scientific Reports* **9**, 19020 (2019).

[46] Giannessi, L. A step closer to compact x-ray lasers. *Nature* **595** (2021).

[47] Schramm, U. *et al.* First results with the novel petawatt laser acceleration facility in Dresden. *Journal of Physics: Conference Series* **874**, 012028 (2017). URL `http://iopscience.iop.org/1742-6596/874/1/012028http://stacks.iop.org/1742-6596/874/i=1/a=012028?key=crossref.f78735833caa4c61b54ae6ac473f2070https://iopscience.iop.org/article/10.1088/1742-6596/874/1/012028`.

[48] André, T. *et al.* Control of laser plasma accelerated electrons for light sources. *Nature communications* **9**, 1–11 (2018).

[49] Irman, A. *et al.* Improved performance of laser wakefield acceleration by tailored self-truncated ionization injection. *Plasma Physics and Controlled Fusion* **60**, 044015 (2018). URL `http://iopscience.iop.org/article/10.1088/1361-6587/aaaef1http://stacks.iop.org/0741-3335/60/i=4/a=044015?key=crossref.aafab0bf34c42950e5342fa74484676dhttps://iopscience.iop.org/article/10.1088/1361-6587/aaaef1`.

[50] Labat, M. *et al.* Interferometry for full temporal reconstruction of laser-plasma accelerator-based seeded free electron lasers. *New Journal of Physics* **22**, 013051 (2020). URL `https://doi.org/10.1088/1367-2630/ab6878`.

Methods

Laser System

The DRACO Ti:Sa chirped pulse amplification system is a dual beam (1 PW and 100 TW) laser system [51]. The system delivers pulses of $\sim 30\,\mathrm{fs}$–FWHM duration at 800 nm central wavelength. In the present experiment, the 100 TW arm is used, delivering 2.1 J on target. An off–axis parabolic mirror (f/20) focuses the laser beam into the gas target, 2.5 mm above the nozzle. Before experiments, a wavefront sensor (PHASICS SID4) in closed loop with a deformable mirror provides focal spot optimization, resulting in a spot size of 21 μm–FWHM measured at the vacuum focus position, and yielding a normalized vector potential a_0 of 2.6. The spectral phase is measured with spectral-phase interferometry for a direct electric field reconstruction (SPIDER-A.P.E.) in parallel with self-referenced spectral interferometry (WIZZLER-fastlite) in closed loop with an acousto-optic programmable dispersive filter (DAZZLER-fastlite) for correction of dispersion mismatch along the laser amplifier and laser beam transport chain. The LPA performance is further optimized by phase correction on the second order (group velocity) dispersion at the DAZZLER. Active beam stabilization within the amplification system in conjunction with online diagnostics for laser near–field and far–field monitoring at the experimental area ensures shot–to–shot pointing stability.

Laser Plasma Acceleration

The laser wakefield accelerator [52] is operated in a tailored scheme of the self-truncated ionization injection regime [53] detailed in [54]. A 2.5 mm diameter supersonic gas nozzle (SourceLAB SL-NOZ), mounted on a fast gas valve (Parker 9-series) provides the gas medium. The gas–jet profile is characterized with an interferometric method [55], yielding a flat top region of $\approx 1.1\,\mathrm{mm}$ with a gas density of $1.4 \times 10^{18}\,\mathrm{cm}^{-3}$ (resulting in a plasma density of $2.8 \times 10^{18}\,\mathrm{cm}^{-3}$) and density ramps of $\approx 0.5\,\mathrm{mm}$ on both sides along the laser propagation axis. A low ionization threshold gas (He), ionized by the main laser preceding pedestal, provides the plasma medium. K-shell electrons of a 1 volume-% fraction high ionization threshold gas (N_2) are only ionized in the vicinity of the laser intensity peak, providing injected electrons which constitute the final electron beam. Injection time is limited by a confined injection volume where the injection conditions are satisfied, governed by the laser- and wakefield-evolution [53]. This scheme nevertheless allows for injection of large quantities of charge, constituting a nanocoulomb-class accelerator where energy spread is minimized by beam loading [56].

LPA beam characterization

The electron beam spectrometer at the LPA exit consists of a 0.4 m long permanent magnet dipole with a magnetic field strength of 0.9 T. Phosphor-based scintillating screens (CAWO-OG-16 FRONT), imaged onto 12-bit CMOS cameras (Basler acA2040-35gm), are positioned such that the energy resolution is optimized with point-to-point imaging [51] from 60 to 270 MeV. The absolute charge response of these scintillating screens was calibrated using the ELBE (Electron Linac for beams with high Brilliance and low Emittance) accelerator [57]. This broad-range spectrometer enables to determine the electron beam spectral distribution and divergence in the horizontal, i.e. non-bending axis plane. Being a destructive beam diagnostic, it can be inserted on demand on the beam path, but is removed for beam transport through the COXINEL beamline.

Beamline magnetic components

The COXINEL beamline starts with a triplet of high gradient permanent magnet based quadrupoles with variable gradient (QUAPEVAs) [58] placed 4.5 cm from the gas jet. Their characteristics, as in magnetic length and gradient, are as follows: (40.7 mm, 171.706 T.m^{-1}), (44.7 mm, -152.18 T.m^{-1}) and (26 mm, 131.82 T.m^{-1}). The chicane consists of four electro-magnet dipoles. The current applied to each dipole is 33.15 A leading to an R_{56} of 1.8 mm. It is the minimum R_{56} allowing for the insertion of the seed injection mirror. The electromagnetic quadrupoles further downstream have a magnetic length of 213 mm each, with a strength of: -1.0737 T.m^{-1}, 3.3388 T.m^{-1}, -9.1712 T.m^{-1} and 4.2974 T.m^{-1}, respectively. The electromagnetic dipole used to dump the beam is operated with a current of 100 A.

Undulator

The radiation source is a planar in-vacuum hybrid undulator consisting of 97 periods of 20 mm length. It was built

319 using NdFeB magnets and Vanadium Permendur poles, and optimized at Synchrotron SOLEIL. Using a series type C
320 Hall probe and a rotating coil, the phase error and electron trajectory have been optimized. The measured magnetic
321 field B_u (first harmonic) versus undulator gap g can be fitted according to: $B_u = 2.58 \exp\left[-3.37\frac{g}{\lambda_u} + 0.095\left(\frac{g}{\lambda_u}\right)^2\right]$
322 in agreement with RADIA [64] simulations. The undulator deflection parameter K_u can be derived from B_u according
323 to: $K_u = 0.9338 \times B_u[T] \times \lambda_u[cm]$. With the minimum gap of 4 mm, the maximum K_u is 2.47.

Electron beam transport method

325 The magnetic elements and the diagnostics have been aligned with a laser tracker and a teodolite on the laser axis
326 using the main laser cross shape references with an accuracy of ±0.025 mm. To transport the electron beam, a beam
327 pointing alignment compensation (BPAC) method [59] relying on the transport matrix response has been used to
328 compensate for an initial electron beam pointing or eventual misalignments of the QUAPEVAs magnetic axis. Position
329 and dispersion along the line can be independently corrected, thanks to a modification of the QUAPEVAs magnetic
330 center via the translation tables on which they are mounted. Finally, the strength of the QUAPEVAs (by a modification
331 of rotating cylindrical permanent magnets) is adjusted to correctly set the electron beam transported energy. The
332 electron beam transport along COXINEL beamline can be simulated with BETA [60] and ELEGANT [61] codes (see
333 Extended Data Fig. 7).

Electron beam diagnostics

335 Five electron beam imagers are implemented along the beamline. They all consist of a scintillating screen, an imaging
336 optics and a camera. The screens are mounted on a motorized stage for on-demand insertion on the electron beam
337 axis and finally back-side imaged. The screen of the first imager (at LPA exit) is a LANEX protected by a 75 μm black
338 ionized Aluminium foil. It is imaged with a pair of simple focusing lenses onto a 12-bit CCD camera (Basler acA640).
339 The magnification ratio (0.12 and 0.17 resp. in the horizontal and vertical plane) together with the screen lead to a
340 resolution of about 150 μm. All downstream imagers are equipped with a 16-bit CMOS camera (HAMAMATSU, ORCA
341 Flash 4.0). The screen of the second imager (in the chicane) is a YAG:Ce protected by a 25 μm black ionized Aluminium
342 foil while the imaging optics is a QIOPTIC custom objective, providing a resolution of about 4.7 μm in both planes.
343 The screens of the third and fourth imagers (at entrance and exit of the undulator) are YAG:Ce while their imaging
344 optics is a f/2 100 mm focal length ZEISS macro objective. The resolution is 6.0 μm (resp. 6.4 μm) in the horizontal
345 (resp. vertical) plane at undulator entrance and 6.5 μm (resp. 6.8 μm) in the horizontal (resp. vertical) plane at
346 undulator exit. The screen of the last imager (after dump dipole) is a LANEX protected by a 25 μm black ionized
347 Aluminium foil while the imaging optics is a f/2.8 105 mm focal length SIGMA macro objective. The resolution is 21 μm
348 in both planes.

349 Two absolute charge monitors, turbo Integrating Current Transformers (ICTs) from BERGOZ, are installed at the
350 entrance (just after LPA chamber) and at the exit (just after undulator) of the beamline.

Seed

352 A small fraction of the LPA driver laser is extracted from its center axis using a 1/2 inch pick–off mirror to generate
353 the seed by frequency conversion. A half-λ plate combined with reflective thin polarizing plates allows step-less
354 adjustment of the frequency conversion input energy from 0.05 up to 1.2 mJ. Frequency tripling is achieved using
355 a set of two BBO-crystals (type 1 SHG & type 1 THG) in combination with a group velocity delay compensation
356 plate and a dual waveplate (EKSMA femtokit). Discriminative spectral filtering for frequency tripled component
357 is achieved using a dichroic mirror and propagation over nine laserline mirrors (262-266 nm, Thorlabs NB1-K04). A
358 broadband spectrometer (Avantes StarLine AvaSpec - ILS2048CL-EVO) confirms no remaining of fundamental or second
359 harmonic contribution in the final seed. The seed has a central wavelength of $\lambda_{\text{seed}} = 269$ nm with a bandwith of
360 $\Delta\lambda_{\text{seed}} = 3.9$ nm–FWHM, measured at the undulator exit (see Fig.2). To relax synchronization, the seed is stretched
361 by introducing temporal dispersion. The total thickness of the FuSi optical elements is $d = 59.9$ mm. Taking into
362 account the group velocity dispersion GVD of FuSi at 270 nm, $D = -4945.5$ ps/(nm.km), the final group delay
363 dispersion is $D_\lambda = D \times d = -0.296$ ps/nm. In other terms, the seed laser pulse experiences a second-order dispersion
364 $D_2 = 1.146 \times 10^4$ fs^2. Assuming an initial pulse duration of 30 fs–FWHM, being Fourier limit, the final seed pulse

365 duration is estimated to be $\Delta T_{seed} = D_\lambda \times \Delta\lambda_{seed} \sim 1$ ps–FWHM. Both ΔT_{seed} and D_2 are used as input parameter
366 for simulations. Spatial filtering is performed after frequency tripling using a lens ($f = 922$ mm) combined with a
367 210 μm diameter ceramic pinhole. A second lens ($f = 461$ mm) collects the beam and projects a weak focus with
368 a Rayleigh length of $z_R = 15$ m and a waist located 5 m before undulator entrance. The seed is injected into the
369 COXINEL beamline using a flat enhanced Aluminium mirror inserted in the middle of the chicane. Using a calibrated
370 photodetector (GENTEC PE10B-Si-D0), the seed energy is measured to be 0.8 μJ at the entrance and 0.5 μJ at the exit
371 of COXINEL beamline.

372 3D overlap adjustment

373 The interaction, i.e. energy exchange, between the seed and the electron beam inside the undulator requires an overlap
374 in three dimensions: space, frequency and time. Spatial overlap is achieved using the near–field imaging system on
375 both the UV–camera (for horizontal) and the UV–spectrometer (for vertical) while steering both the seed and the
376 electron beam. Since the distance between the two lenses of the imaging system can be remotely adjusted to change
377 the object plane, the spatial overlap can be monitored all along the undulator. The frequency overlap is achieved
378 using the spectrometer while tuning the undulator gap. Since both seed and electron beam originate from the same
379 laser, they are inherently synchronized and free of jitter. The remaining delay τ is adjusted using a delay stage on the
380 seed path while monitoring the arrival times of seed and synchrotron radiation with a streak camera (HAMAMATSU,
381 FESCA–100). For this purpose, seed and synchrotron radiation can be extracted at the undulator exit using a removable
382 Aluminium mirror, and further focused using a FuSi lens ($f=1$ m) into the streak camera entrance slit. Seed and
383 synchrotron radiation pulses are simultaneously observed in single–shot while adjusting the delay stage on the seed
384 path, until temporal overlap falls beyond the accessible resolution ($\approx$500 fs).

385 Photon beam diagnostics

386 The main radiation diagnostics are located after the dump dipole at the end of the beamline. The radiation is
387 collected by a pair of lenses: one plano–convex FuSi of focal length $f=400$ mm followed by one plano–concave FuSi
388 of focal length $f=-200$ mm. Depending on the distance between the two lenses, this optical system can image the
389 radiation from the undulator entrance to undulator exit on to a fixed image plane downstream. In this fixed image
390 plane, two diagnostics can be implemented: a UV-camera or a 2D spectrometer depending on the position of a final
391 motorized enhanced Aluminium mirror. The UV-camera is an ORCA-II from HAMAMATSU. The spectrometer is an
392 iHR320 from HORIBA/JOBIN–YVON equipped with a back–illuminated camera, providing with spectral distribution along
393 the horizontal axis and spatial distribution along vertical axis.

394 FEL simulation

395 The spatio–spectral distribution of the FEL at the undulator exit is simulated in four steps. In a first step, a 6D
396 Gaussian electron beam distribution with 10^6 particles is generated using a set of RMS values for beam position,
397 divergence, energy spread, duration and giving a total bunch charge. As second step, this 6D distribution is then
398 transported down to the undulator entrance with the BETA code, using a chromatic matching lattice set at 188.8 MeV.
399 Transporting with this code or ELEGANT is equivalent (See Extended Data Fig. 8). The 6D distribution obtained at
400 the undulator entrance is longitudinally sampled into 2000 slices, while each slice is described by the six RMS values of
401 its envelope. The duration of one slice is $4 \times \lambda_{seed}$, i.e. 3.6 fs. In parallel, the seed is simply modeled in the frequency
402 domain according to its central wavelength λ_{seed} of 269 nm, bandwidth $\Delta\lambda_{seed}$ of 3.9 nm–FWHM and group delay
403 dispersion D_λ of -0.296 ps/nm. After Fourier transform, the seed pulse in the time domain is sampled into 2000
404 slices, while each slice is described by its peak power and phase. As third step, both the seed and the electron beam
405 longitudinal distributions are loaded into the GENESIS [62] code to simulate the radiation generation process along
406 the undulator. The result of this simulation is the 3D (x, y, t) electric field at the undulator exit, with x (resp. y)
407 the coordinate along the horizontal (resp. vertical) plane and t the longitudinal (time) coordinate. Using standard
408 Fourier optics, the 2D ($x=0$, y, t) field distribution is finally converted into the 2D (y, λ) spatio–spectral distributions
409 illustrated in Fig. 2. The simulated spatio–spectral distributions can be compared directly to the spatio–spectral
410 distribution recorded on the UV–spectrometer.

411 FEL analytical modeling

412 The FEL emission is observed to be red-shifted with respect to the seed wavelength. This red-shift $\Delta\lambda_{FEL}$ can be
413 attributed to a stretching of the initial density modulation (at λ_{seed}) along the undulator and is proportional to the
414 undulator and chicane dispersion ratio according to [63]:

$$\Delta\lambda_{FEL} = \frac{(1 + K_u^2/2)L_{eff}}{\gamma^2 R_{56}} \lambda_{seed}. \tag{2}$$

415 However, this simple formula does not take into account the time dependence of the electron beam energy as well
416 as the dispersion of the seed laser pulse. After passing through the chicane, the energy of the electrons $mc^2\gamma(t)$ is
417 linearly correlated to their longitudinal position t according to:

$$\gamma(t) = \gamma_0 + \frac{c\gamma_0}{R_{56}}t, \tag{3}$$

418 where t is the longitudinal position along the beam with respect to the central energy $mc^2\gamma_0$. Due to the dispersion
419 introduced by the optical elements, the seed laser is chirped and the instantaneous seed wavelength also depends on
420 t according to:

$$\lambda_{seed}(t, \tau) = \lambda_0 + \frac{t - \tau}{D_\lambda}, \tag{4}$$

421 where λ_0 is the seed central wavelength and τ is relative delay between the seed laser pulse and the electron beam.

422 To fulfil the undulator resonance condition, the FEL interaction can only occur at the longitudinal position t_0 where

$$\lambda_R(t_0) = \frac{\lambda_u(1 + K_u^2/2)}{2\gamma(t_0)^2} = \lambda_{seed}(t_0), \tag{5}$$

423 i.e. at:

$$t_0 = \frac{\tau}{D_\lambda} \times \left[\frac{1}{D_\lambda} + \frac{\lambda_u c(1 + K_u^2/2)}{\gamma_0^2 R_{56}} \right]^{-1}. \tag{6}$$

424 Taking into account the time dependence of the undulator resonance condition into Eqs.(2, 3, 4) permits to refine the
425 expression of the red-shift FEL emission:

$$\Delta\lambda_{FEL}(\tau) = \frac{(1 + K_u^2/2)L_{eff}}{\gamma(t_0)^2 R_{56}} \left(\lambda_0 + \frac{t_0 - \tau}{D_\lambda} \right), \tag{7}$$

426 as a function of the relative delay τ between the seed laser and the electron beam.

427 **FEL data analysis**

428 Both measured and simulated raw FEL data correspond to a single–shot 2D spatio–spectral distribution at the
429 undulator exit. Experimental images correspond to the UV–spectrometer records using the near–field imaging system
430 while simulated images correspond to the Fourier transform of the 3D electric field simulated by GENESIS. From those
431 images, ξ_{FEL} and λ_{FEL} are systematically extracted as follows.

432 Each measured image is processed to remove the camera sensor offset and the hot–pixels from Bremsstrahlung
433 radiation. A preliminary record of Synchrotron Radiation (SR) signal alone, i.e. without seed, enables to identify
434 the vertical position of the expected FEL signal, which defines the $y = 0$ position. The FEL spectral profile $I_{FEL}(\lambda)$
435 is then obtained from vertical integration over a region of interest of ± 6 pixels (corresponding to ± 156 μm) around
436 $y = 0$ and is normalized to its maximum value. The reference seed spectral profile $I_{seed}(\lambda)$ is deduced from the same
437 image, integrating similarly the signal over the same pixel range but 30 pixels away from $y = 0$, and then normalizing
438 to the maximum value. Each simulated image is treated exactly the same way to extract both FEL and seed simulated
439 spectral profiles.

The following process is then applied to both measured and simulated spectral profiles. The FEL signal–to–noise ratio SNR_{FEL} is defined as

$$SNR_{FEL}(\lambda) = \frac{I_{FEL}(\lambda) - I_{seed}(\lambda)}{I_{seed}(\lambda)} \tag{8}$$

and fitted with a Gaussian function for an accurate retrieval of the FEL wavelength λ_{FEL} (location of maximum SNR_{FEL} along λ). The FEL differential signal, corresponding to the FEL spectra with seed subtraction, is defined as follows:

$$\Delta_{FEL}(\lambda) = I_{FEL}(\lambda) - I_{seed}(\lambda) \tag{9}$$

and its integral within the spectral interval [λ_1=239 nm ; λ_2=279 nm] gives:

$$\xi_{FEL} = \int_{\lambda_1}^{\lambda_2} \Delta_{FEL}(\lambda')d\lambda', \tag{10}$$

i.e. the energy (arb. units) of the isolated FEL pulse.

Data availability

All data are available upon reasonable request from the corresponding authors.

Code availability

Codes used in this study are available upon reasonable request from the corresponding authors.

[51] Schramm, U. et al. First results with the novel petawatt laser acceleration facility in Dresden. Journal of Physics: Conference Series 874, 012028 (2017).

[52] Tajima, T. & Dawson, J. M. Laser Electron Accelerator. Physical Review Letters 43, 267270 (1979).

[53] Zeng, M., Chen, M., Sheng, Z.-M., Mori, W. B. & Zhang, J. Self-truncated ionization injection and consequent monoenergetic electron bunches in laser wake- field acceleration. Physics of Plasmas 21, 030701 (2014).

[54] Irman, A. et al. Improved performance of laser wakefield acceleration by tailored self-truncated ionization injection. Plasma Physics and Controlled Fusion 60, 044015 (2018).

[55] Couperus, J. et al. Tomographic characterisation of gas-jet targets for laser wakefield acceleration. Nuclear Instruments and Methods in Physics Research Section A: Accelerators, Spectrometers, Detectors and Associated Equipment 830, 504509 (2016).

[56] Couperus, J. P. et al. Demonstration of a beam loaded nanocoulomb-class laser wakefield accelerator. Nature Communications 8, 487 (2017).

[57] Kurz, T. et al. Calibration and cross-laboratory implementation of scintillating screens for electron bunch charge determination. Review of Scientific Instruments 89, 093303 (2018).

[58] Marteau, F. et al. Variable high gradient permanent magnet quadrupole (quapeva). Applied Physics Letters 111, 253503 (2017). Ghaith, A. et al. Tunable high gradient quadrupoles for a laser plasma acceleration based fel. Nuclear Instruments and Methods in Physics Research Section A: Accelerators, Spectrometers, Detectors and Associated Equipment 909, 290293 (2018).

[59] André, T. et al. Control of laser plasma accelerated electrons for light sources. Nature communications 9, 111 (2018).

[60] Payet, J. et al. Beta code. CEA, SACLAY. http://irfu.cea.fr/Sacm/logiciels/index6.php.

[61] Borland, M. Elegant: A flexible sdds-compliant code for accelerator simulation. Tech. Rep., Argonne National Lab., IL (US) (2000).

[62] Reiche, S. Genesis 1.3: a fully 3d time-dependent fel simulation code. Nuclear Instruments and Methods in Physics Research Section A: Accelerators, Spectrom- eters, Detectors and Associated Equipment 429, 243-248 (1999).

[63] Labat, M. et al. Interferometry for full temporal reconstruction of laser-plasma accelerator-based seeded free electron lasers. New Journal of Physics 22, 013051 (2020).

[64] Chubar, O. et al. A three-dimensional magnetostatics computer code for insertion devices. Journal of synchrotron radiation 5, vol.3, 481-484 (1998).

Acknowledgements

Author contributions

The LPA based FEL activity was launched by M.E.C and V.M. in a SOLEIL/LOA collaboration, with M.E.C. responsible for the COXINEL project and S.C., O.K. and C.T. of the LPA. After test experiments with S.C., M.E.C., M.E.A., J.G., A.G., N.H., O.K., M.Labat, A.L., D.O.E., P.R., E.R. and C.T. using the LOA LPA, it was decided to move the line to HZDR in the frame of a new collaboration. For the present experiment, A.I. and U.S. are responsible for the LPA project at HZDR. The COXINEL experiment with HZDR LPA was prepared by F.Bl., J.P.C.C., M.E.C., C.E., A.G., S.G., C.H., M.Labat and A.L. The COXINEL beamline has been designed at SOLEIL by A.L. for the electron beam transport, M.Labat for the FEL calculations, A.B. and K.T. for the mechanics. The different components of the line have been prepared at SOLEIL (modification of the QUAPEVA for HZDR vacuum constraints (A.B., P.B., F.Bl., J.P.D., C.H., C.K., M.H.N., J.V.), electromagnets (F.Br., F.M., M.V.), power supplies (F.Bo, Y. D.), undulator (P.B., F.Bl., M.V., J.V.), diagnostics (M.Labat, N.H., M.E.A., J.P.R), vacuum (J.P.D., C.K., M. Van.), server (S. L.), electronics (F. Bl.)). A.B., P.B. F.Bl., F.Br., J.P.C.C., M.E.C., C.De O., Y.D., C.E., A.G., S.G., A.I., C.K., M.Labat, M.LaB., B.L., D.P., M.S., K.T., P.U., M.Val. and M.Van. contributed to the installation and the alignment of the COXINEL beamline at HZDR, with P.E. and M.K. for the synchronization and timing diagnostics. During the experiments at HZDR, S.B., R.G., U.H., T.P. operated the DRACO laser system, J.P.C.C., M.E.C., M. El A., A.G., N.H., A.I., O.K., M.Labat, M.LaB., A.L., E.R., S.Sch, P.U., Y.Y.C. participated to the experimental sessions. J.P.C.C., A.G., M.Labat and E.R. analyzed the experimental data. LPA PIC simulations were performed by A.D., R.P. and K.S., electron beam transport simulations by A.G., A.L., M.Labat and E.R., FEL GENESIS simulations by M.Labat and E.R., the FEL analytical model was refined by M.Labat and E.R. J.P.C.C., M.E.C, A.G., A.I., M.Labat, E.R. and U.S. co-wrote the paper. The results were jointly discussed by S.C., J.P.C.C., M.E.C., A.G., A.I., O.K., M.Labat, E.R., U.S. and C.T.

Competing interests

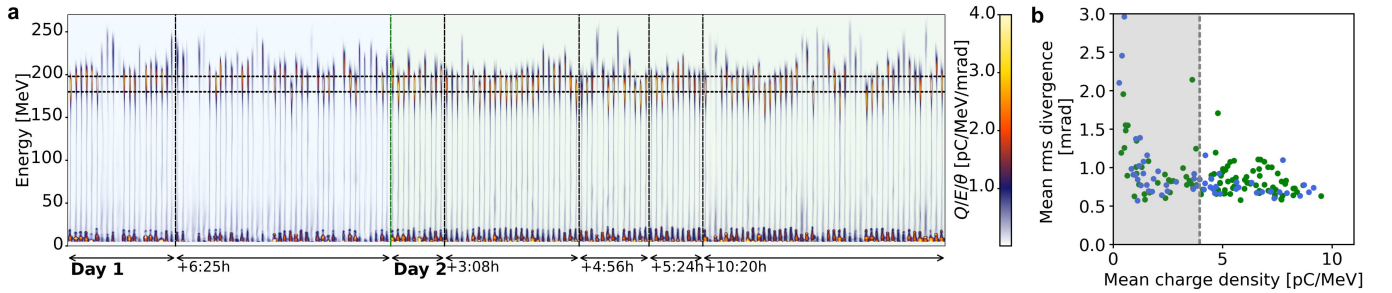The authors declare no competing interests.

FIG. 5. **Electron beam properties at the entrance of COXINEL beamline**. **(a)** the charge distribution of several sets of sequential shots at different times over two experimental days. No discrimination or sorting for performance is applied. **(b)** the mean RMS divergence and mean charge density evaluated for the $\pm 5\%$ energy range (180–198 MeV) around the COXINEL design central energy (189 MeV) for all shots from a). Selecting shots considered to be of sufficient quality to contribute to FEL amplification, with a mean charge density > 4 pC/MeV throughout the abovementioned energy range (indicated by *dashed box*), selects 60% of all shots, consistent with experimental observations on FEL amplification signal probability per shot. Considering selected shots, a mean charge density of (6.3±1.4 s.d.) pC/MeV with a mean RMS divergence of (0.80±0.17 s.d.) mrad is found.
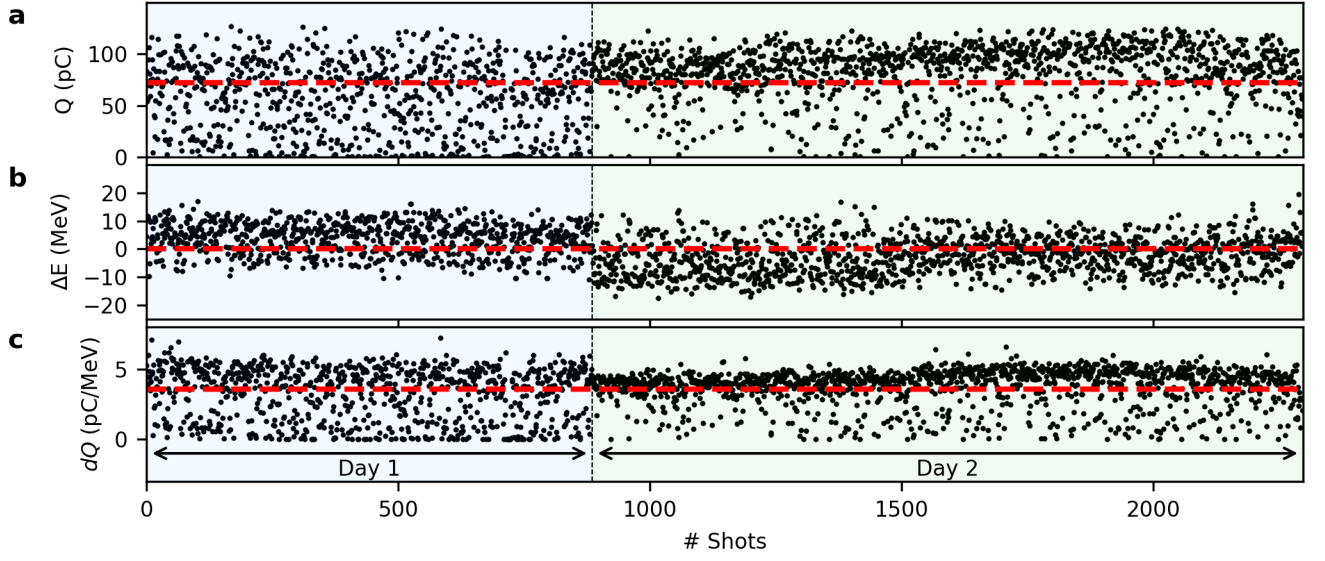
FIG. 6. **Electron beam properties at the exit of COXINEL beamline**. **a**, Charge Q measured at beamline exit. **b,c**, Data analysis from last beamline imager after dipole dump. Images are calibrated along horizontal axis into energy, providing with the shot–to–shot energy variation ΔE with respect to the mean central energy (**b**). Charge density dQ (**c**) is deduced from Q and ΔE. Data collected during the two days of FEL experiments.
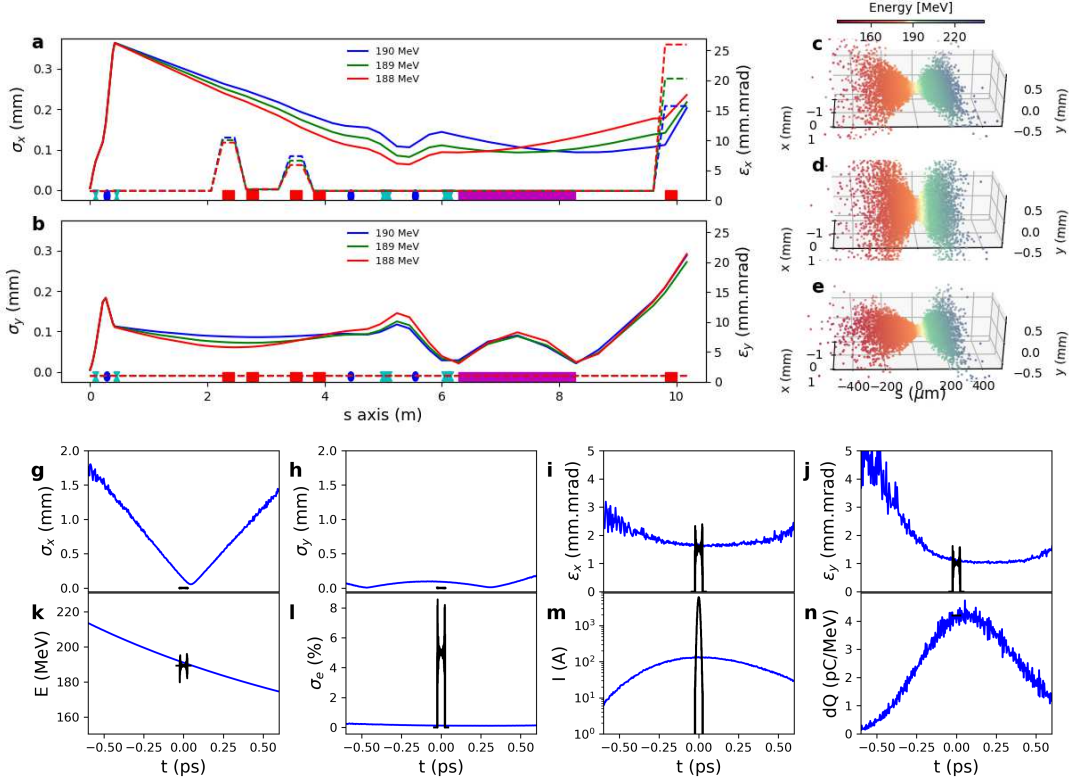
FIG. 7. **Electron beam transport**. **a, b**, COXINEL beamline lattice for chromatic matching in horizontal (**a**) and vertical (**b**) planes, with electron beam sizes (*solid lines*) and normalized emittances (*dashed lines*) for different energies. **c, d, e**, Electron beam phase–space at undulator entrance (**c**), middle (**d**) and exit (**e**). **g-n**, Electron beam longitudinal properties at source point (*black lines*) and entrance of undulator (*blue lines*). Transport calculation with ELEGANT and BETA using following beam parameters at source point: E_e=188.8 MeV, charge Q=100 pC, σ_z=2 μm–RMS, normalized emittance $\epsilon_{x,y}$=(1.5;1.0) mm.mrad, divergence $\sigma_{x',y'}$=(1.5;1.0) mrad–RMS, $\sigma_e = 5\%$–RMS, with QUAPEVA 2 strength detuned by -2% and R_{56}=1.8 mm.
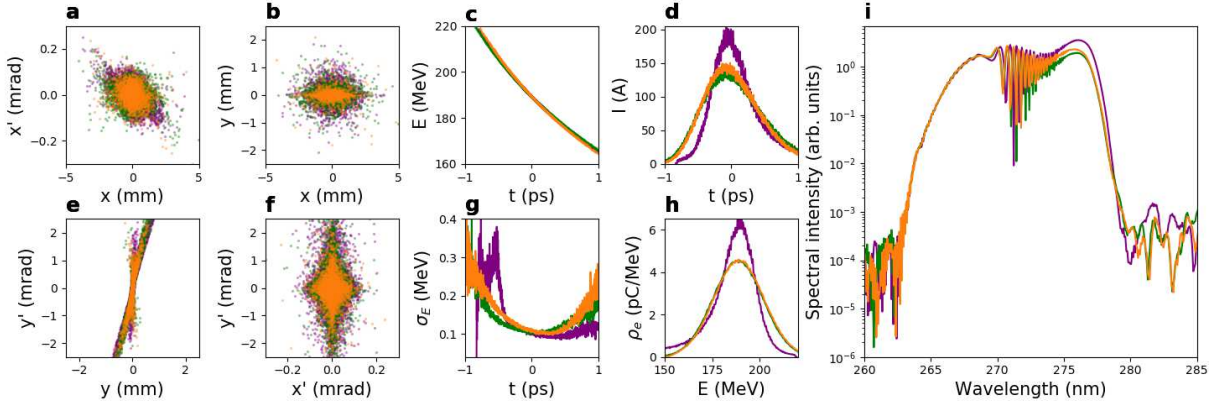

FIG. 8. **Electron beam transport method comparison and consequence on FEL performance. a–h** Electron beam properties at undulator entrance: transverse phase–spaces (**a,b,e,f**) ; energy (**c**), current (**d**) and slice energy spread (**g**) longitudinal distributions ; charge density versus energy (**h**). Electron beam transported using BETA code with a Gaussian beam distribution at source point in (*orange*), using ELEGANT with same Gaussian beam at source point in (*green*) and using ELEGANT with electron beam energy and divergence distributions measured on the electron beam spectrometer (*purple*). Parameters for Gaussian beam definition at source point: $E_e = 189$ MeV, $\sigma_e = 7\%$–RMS, divergence: $\sigma_{x'} = 0.85$ mrad–RMS and $\sigma_{y'} = 0.57$ mrad–RMS, normalized emittance: $\varepsilon_x = 1.5$ mm.mrad and $\varepsilon_y = 1.0$ mm.mrad, $\beta_x = 0.00562$ m, $\beta_y = 0.00843$ m, $\sigma_z = 1\mu$m–RMS.
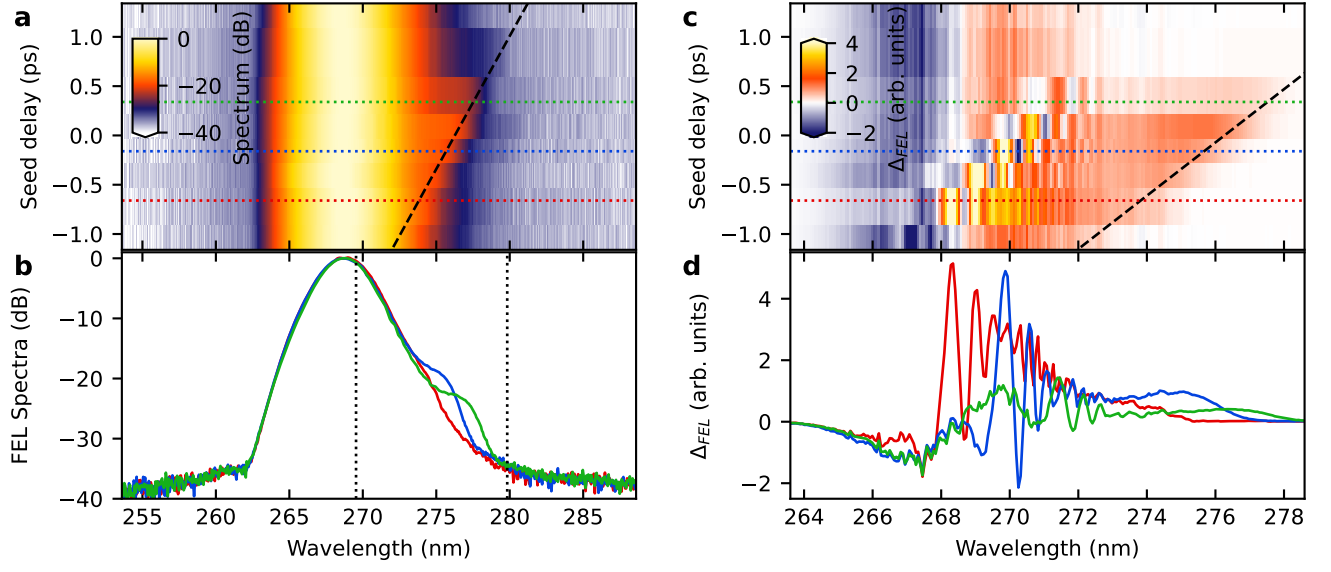
FIG. 9. **Seed delay scan. a,b.** Average FEL spectra versus seed delay. **c,d.** Average FEL differential signal $\Delta_{FEL}(\lambda)$ (FEL spectra with seed subtraction) versus seed delay. **b,d.** Spectra for three seed delays: -0.66 ps (red), -0.16 ps (blue), and 0.34 ps (green). Black dashed line (**a,d**): analytical model for FEL wavelength red shift. Vertical dotted lines (**b**): bandwidth for integration of the FEL and seed intensity.